

TEXTURE AND HARDNESS IN WIRE DRAWN [001] COPPER SINGLE CRYSTALS

A. BORBÉLY^{a,*}, L.S. TÓTH^b and B. BOLLE^c

^a*Institute for General Physics, Eötvös University, Budapest, Múzeum krt. 6–8, H-1088, Hungary;* ^b*Laboratoire de Physique et Mécanique des Matériaux,* ^c*Laboratoire d'Étude des Textures et Applications aux Matériaux, Université de Metz, ISGMP, Ile du Saulcy, 57045 – Metz cedex 01, France*

(Received 10 February 1998)

The crystallographic texture and Vickers hardness which develop during wire-drawing of [001] oriented copper single crystals have been studied experimentally as well by simulations. The experiments revealed orientation changes producing cross-shaped patterns in the {200} pole figures and important variations in the Vickers hardness across the diameter. Metallographic investigations showed the presence of deformation bands perpendicular to the initial <100> directions. By adopting a model for the velocity field inside the die, simulations have been carried out by using a Taylor type rate sensitive crystal plasticity model, including microscopic hardening. The simulated pole figures show the features of the experimental ones and the predicted stress levels correlate well with the measured hardness data.

Keywords: Wire drawing; Texture; Pole figure; Microhardness; Viscoplastic crystal plasticity

INTRODUCTION

Cold drawing is an important technological method to obtain wires of small diameters. This process consists of numerous passes, during which the material is drawn through several dies of successively decreasing diameters. Large plastic deformations can be achieved by this forming process, which can therefore involve severe strain hardening as shown

* Corresponding author. Institut für Werkstoffwissenschaften, Lehrstuhl I, Universität Erlangen – Nürnberg, Martens str 5, D-91058 Erlangen, Germany.

by Gil Sevillano *et al.* (1980). It is difficult, however, to measure flow stress in wire drawing, because of the friction forces between the wire and the die. The hardening state of the material can also depend on the radius. In such conditions, microhardness measurements are useful in order to access the hardening characteristics of the material.

Because of the large strains during wire drawing, grain orientations change progressively and preferred orientations (texture) appear. Strong textures are indicators of anisotropy, which can be studied with conventional pole figure measurements. Thus, in order to understand better the deformation process, texture measurements can also be very useful.

The texture changes which take place in wire drawn polycrystals as well as in single crystals were the subject of several earlier studies by Ahlborn (1965a,b; 1966), Ahlborn and Sauer (1968), Mathur and Dawson (1990), Montesin *et al.* (1991), Sugondo *et al.* (1991) and Van Houtte *et al.* (1994). Ahlborn (1965a,b; 1966) has examined the textures which develop from different initial orientations of f.c.c. single crystals. He found that at moderate strains the preferred orientations are the $\langle 001 \rangle$ and $\langle 111 \rangle$ (parallel to the wire axis).

In the present work, $[001]$ oriented copper single crystals are deformed in wire drawing. The main advantage of studying single crystals is that the boundary conditions of the deformation are well defined, while the deformation of a grain in a polycrystal requires several assumptions on the nature of the interaction between the grain and its neighbors (e.g. Taylor, 1938, or self-consistent models of Molinari *et al.*, 1987). The aim of the experimental part of this work is to explore the hardening state of the material via Vickers hardness measurements, and its anisotropy by pole figure analysis. Finally, for a better understanding of the deformation process, a suitable physical model (Taylor viscoplastic approach) will be employed to predict the hardening states as well as the textures which develop.

EXPERIMENTAL OBSERVATIONS

Sample Preparation and Wire Drawing

Two copper single crystal bars of 4 mm diameter with $[001]$ parallel to the axis of the bar were grown from 5 N copper using the Bridgman

TABLE I Diameters of the dies, D , the cross-sectional area reductions $\Delta A/A_0$, and the corresponding true strains e

Pass Nr.	D (mm)	$\Delta A/A_0$ (%)	e
0	4.00	0	0
1	3.80	10	0.10
2	3.38	29	0.34
3	3.00	44	0.58
4	2.73	55	0.76
5	2.49	61	0.95
6	2.30	67	1.11
7	2.12	72	1.27
8	1.98	75.5	1.41

technique. The crystallographic orientations of both crystals were examined with pole figure measurements and agreed with $[001]$ within 1° . The samples were drawn at a constant velocity of 10 mm/min. in a Zwick tensile test machine at room temperature. Eight passes were done with a die angle 2α of 10° and lubricant was used to reduce friction. The diameters of the dies, the corresponding cross-sectional area reductions and the computed true strains are presented in Table I.

Metallographic Investigations

The deformed samples were examined metallographically on two surfaces: one which is perpendicular to the drawing direction, called "axial case" (see Fig. 1(a)), and another, made parallel to the sample axis, called "side case" (see Fig. 1(b)). The samples were chemically polished in a solution containing equal proportions of Struers OP-S and another mixture made of 500 ml H_2O , 500 ml C_2H_5OH and 10 g Fe_2N_3 . In order to make the slip line pattern visible, chemical etching was applied using the technique described by Pokorny and Pokorny (1967). Pictures were taken with the help of a Zeiss optical interference microscope.

As it can be seen from the micrographs of Fig. 1, both the axial and the side surfaces show clear deformation bands. In Fig. 1(a), the bands display a symmetrical pattern having a four-fold symmetry around the wire axis. The orientation of the bands were determined from pole figure measurements and they were found to be aligned almost perpendicular either to the $[100]$ or to the $[010]$ directions. In Fig. 1(b), the deformation bands appear parallel to the sample axis, from which it can be concluded that these bands are continued all along the sample.

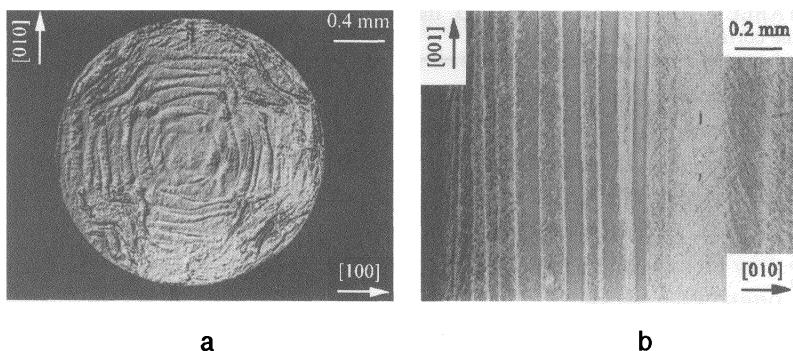


FIGURE 1 Metallographic pictures taken from the sample experiencing 7 passes (strain: $e = 1.27$) showing (a) cut perpendicular to the drawing axis [001], (b) cut parallel to the drawing axis.

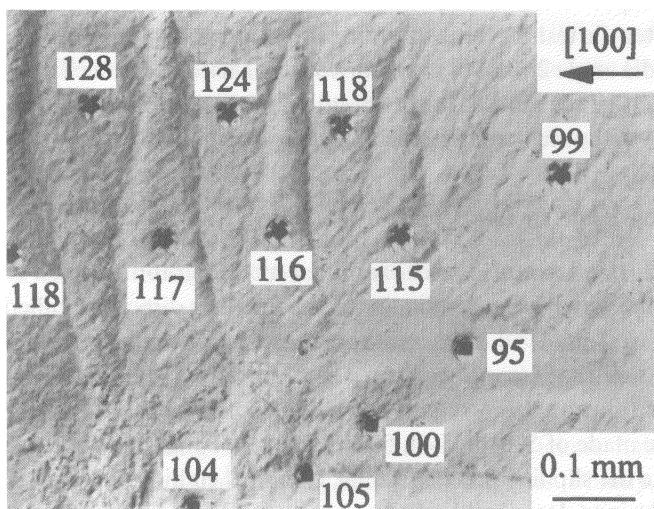


FIGURE 2 Indentations together with the corresponding Vickers hardness values. The hardness is different in adjacent bands and also between the [100] and [110] directions (strain: $e = 1.11$).

It can also be seen from Fig. 1(b) that the broadness of the bands decreases with the distance from the axis of the sample and that the contrast varies periodically from one band to the next which reveals misorientations between the bands.

Figure 2 shows some deformation bands at a higher magnification together with the indentations made during the microhardness

measurements. In the vicinity of the indentations, slip lines are clearly visible, which are aligned parallel to the $\langle 110 \rangle$ directions. The angle between these slip lines and the deformation bands is close to 45° . At this higher magnification scale in Fig. 2 it can be seen that the deformation bands are not perfectly aligned with the $[100]$ direction. They look like ‘teeth’ of two superimposed ‘combs’. The metallographic picture for the axial case (Fig. 1(a)) suggests an inhomogeneous deformation pattern. In fact, in the $\langle 110 \rangle$ directions, near the surface of the sample, the deformation seems to be more important than elsewhere. The deformation bands are quite straight perpendicular to the $[100]$ or $[010]$ directions, while the bands show more complicated forms in the $\langle 110 \rangle$ directions.

Vickers Hardness Measurements

The heterogeneity of the deformation was quantitatively characterized by Vickers hardness measurements in the cross section of a sample deformed to a true strain of $e = 1.11$. The hardness values were obtained by employing a weight of 0.25 N and were converted into flow stresses using a dividing factor of 3.0, as proposed by Tabor (1951). Measurements have been carried out in two different directions: $[100]$ and $[110]$, starting from the center of the sample. Figure 3 shows the results obtained for the sample deformed to a true strain of 1.11 as a function of the radius. Similar results were obtained for other samples, too.

According to the results shown in Fig. 3, the wire is the softest in its center and is in a more and more hardened state as the radius increases. There are, however, important differences between the hardness values measured along the $[100]$ and $[110]$ directions; the hardness being significantly lower along the radius parallel to the $[110]$ direction.

The hardness is different from one band to another but varies inside of a single band, too. Figure 4 presents the microhardness data obtained within a single deformation band by employing a Shimadzu DUH-202 nano-indenter instrument. Using a weight of 5 mN, the indentation diameter was only about $0.3 \mu\text{m}$, which is in the order of the dislocation cell size expected for this deformation stage (see Gil Sevillano *et al.* (1980)). Figure 4 shows that the hardness is higher at the borders of the band than in its center, which is probably a consequence of the different dislocation densities between these regions.

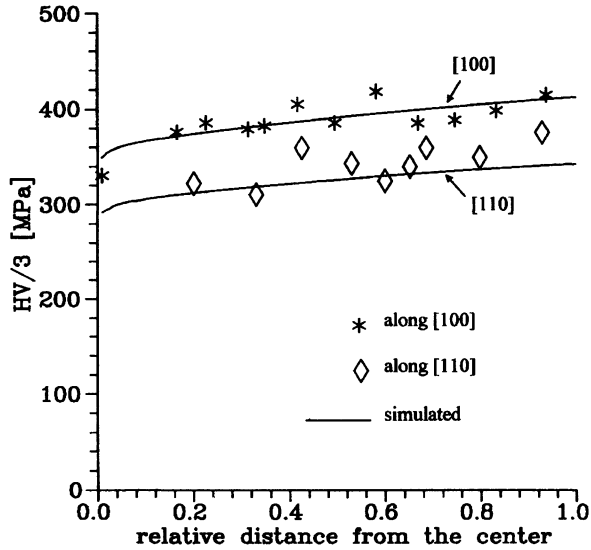


FIGURE 3 Vickers hardness values measured on the sample passing through 6 dies (strain: $\epsilon = 1.11$) taken along the radius in the [100] and [110] directions. The results of the crystal plasticity simulations are also shown with continuous lines.

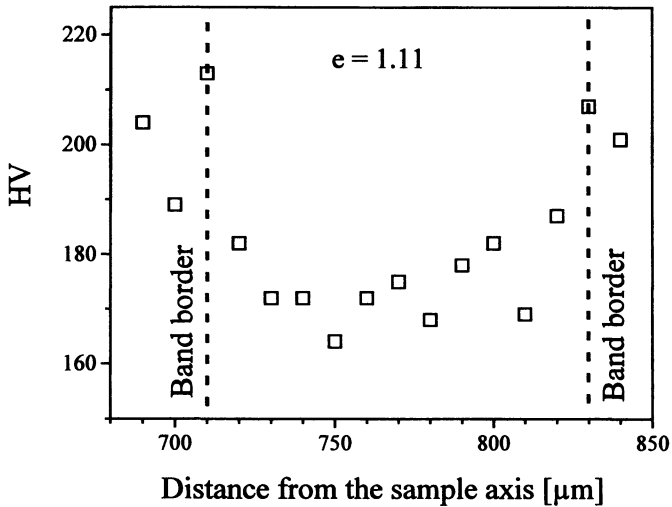


FIGURE 4 Hardness values measured in the [010] direction through a deformation band of picture (1b) with the help of a nano-indenter.

Texture Measurements

Texture measurements have been carried out on the maximum deformed sample (strain of 1.41) on its cross section perpendicular to the longitudinal axis using a multi-pole-figure goniometer with an INEL curved position sensitive detector. λFeK_α radiation was used with a beam size of $1.25 \times 2.5 \text{ mm}^2$. In order to obtain precise information on the distribution of the pole densities, the step size was 1.25° and 5° in tilt and in azimuth, respectively. The measured $\{200\}$, $\{111\}$ and $\{220\}$ pole figures are presented in Fig. 5(a)–(c), respectively. Some small amount of shift of the reflection peaks can be seen in the pole figures which is due to a small deviation of the polished sample surface from the position of perfect perpendicularity to the longitudinal axis.

Before deformation, the measured pole figures showed very concentrated and high intensity peaks (not shown here) as it was expected for an undeformed single crystal. However, it can be seen in Fig. 5(a)–(c) that in the highly deformed state, the intensity distributions are broadened significantly and some important deformations in the intensity distribution of the peaks are also evident. The (002) reflection in the middle part of Fig. 5(a) is definitely cross shaped, and the $\{111\}$ reflections are also elongated in Fig. 5(b) towards the center of the pole figure as well as perpendicularly to the radial directions. The crosses in both measured pole figures are oriented at 45° with respect to the $\langle 001 \rangle$ directions. In the $\{220\}$ pole figures, the pole density

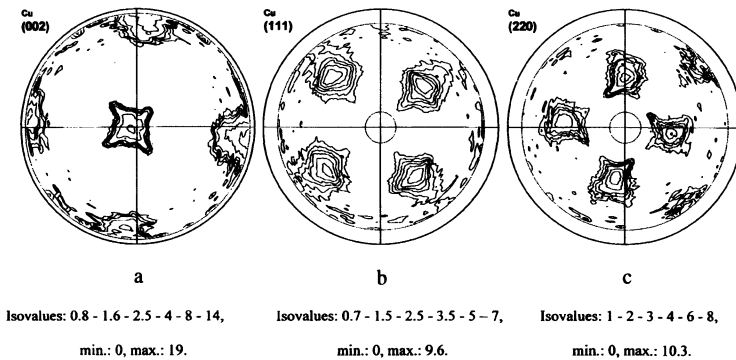


FIGURE 5 Measured pole figures after 8 passes (strain: $e = 1.41$): (a) $\{002\}$, (b) $\{111\}$ and (c) $\{220\}$.

distribution shows also an interesting pattern; a kind of ‘ears’ can be seen at the edge of each maximum.

As the pole figure measurements were carried out globally on the whole sample surface, they can only show average tendencies. The amount of orientation changes may depend on the radius. In fact, detailed investigations of the slip line patterns in the etched sample surfaces showed that the rotation of the crystal axes is definitely higher near the outermost radius of the sample than in the central regions.

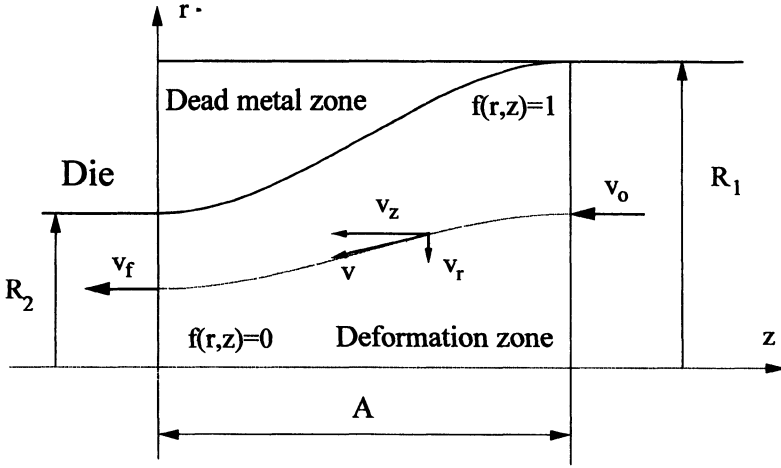
CRYSTAL PLASTICITY MODELING

In order to explain some of the experimental observations, crystal plasticity simulations have been carried out. In the present case – as the specimens are monocrystalline – the boundary conditions for their plastic deformation are relatively well defined, so the Taylor viscoplastic model is perfectly adequate. During wire drawing, each material element follows a certain flow line. This element is part of the original single crystal, which hardens and can change its orientation during its passage in the die. If the flow lines are known, they can be introduced into the crystal plasticity model and the hardening state as well as the orientation changes can be readily calculated. For this purpose, the flow line model of Altan *et al.* (1992) has been used in the present work as it was already successfully employed in earlier polycrystal modeling of wire drawing by Heizmann *et al.* (1996). In what follows, first the main elements of the Altan *et al.* (1992) model will be given, then the crystal plasticity calculations will be described. Finally, the obtained results will be compared to the experimental observations.

The Altan *et al.* Velocity Field in Wire Drawing

Altan *et al.* (1992) described the deformation of the material in wire drawing with the help of flow lines, see Fig. 6. These lines are cubic functions of the z -coordinate and are continuous everywhere, including the entrance and the exit points of the die:

$$f(r, z) = \frac{A^3/(R_1 - R_2)r}{z^2(3A - 2z) + R_2/(R_1 - R_2)A^3} = C. \quad (1)$$

FIGURE 6 A flow line in the Altan *et al.* model.

In this relation, A is the length of the deformation zone in the die, R_1 and R_2 are the radii of the wire before and after the pass, r and z are the radial and axial cylindrical coordinates, respectively, and C defines the position of the flow line within the die (for example, $C=0$ or $C=1$ represents a flow line at the center or at the surface of the die, respectively). The components of the velocity of a material element along a flow line defined in Eq. (1) are given by

$$\begin{cases} v_\theta = 0, \\ v_r = -v_f \left(\frac{R_2}{(R_1 - R_2)A^3} \right)^2 6rz(A - z)(z^2(3A - 2z) \\ \quad + R_2 / (R_1 - R_2)A^3)^{-3}, \\ v_z = -v_f \left(\frac{R_2}{(R_1 - R_2)A^3} \right)^2 (z^2(3A - 2z) + (R_2 / (R_1 - R_2)A^3)^{-2}, \end{cases} \quad (2)$$

where v_f is the velocity of the wire leaving the die. The velocity gradient \dot{d} can be derived from Eq. (2), which leads to 4 non-null components in \dot{d} :

$$\dot{d} = \begin{pmatrix} \partial v_r / \partial r & 0 & \partial v_r / \partial z \\ 0 & \frac{v_z}{r} & 0 \\ 0 & 0 & \partial v_z / \partial z \end{pmatrix}. \quad (3)$$

For the mathematical expressions of the components of $\dot{\mathbf{d}}$, see Appendix. As can be seen from Eq. (3), there is only one shear component, \dot{d}_{rz} . In fact, this component accounts for the changes in the direction of the flow as material travels along the flow line. A possible friction with the die is not accounted for in the model of Altan *et al.* (1992).

The total time for passing through the die along a given flow line can also be readily calculated; see its expression in the Appendix. As the crystal plasticity code is working in an incremental way, this time interval is divided into 100 equal time increments. The numerical code is then supplied with a list of 100 velocity gradient matrices calculated from Eq. (3), each describing the local velocity gradient along the given flow line.

The Crystal Plasticity Model

As discussed above, the velocity gradient along the flow lines is known. It is then possible to calculate the operating slip systems and the orientation changes with the help of the viscoplastic model of crystal plasticity as formulated by Hutchinson (1976) and by Tóth *et al.* (1990). In the crystal plasticity calculations, the usual power law is used, which relates the rate of slip $\dot{\gamma}_s$ with the resolved shear stress τ_s in a slip system identified by the index s (see Tóth *et al.*, 1990):

$$\tau_s = \tau_s^0 \operatorname{sign}(\dot{\gamma}_s) \left| \frac{\dot{\gamma}_s}{\dot{\gamma}_s^0} \right|^m. \quad (4)$$

In this relation, τ_s^0 is a reference shear stress corresponding to the reference slip rate $\dot{\gamma}_s^0$ and m is the strain rate sensitivity exponent. As the material is pure copper, the 12 $\{111\}\langle 110 \rangle$ slip systems were used in the simulations. As for the reference slip rate $\dot{\gamma}_s^0$, it was taken to be 0.033 s^{-1} , which is the same value as the strain rate in the wire drawing tests. Strain rate sensitivity is low in pure copper at room temperature; the value of $m = 0.02$ was employed.

The strain rate tensor $\dot{\epsilon}$ is the symmetric part of the velocity gradient $\dot{\mathbf{d}}$, so in order to obtain the slip distribution at a given time, the

following equation system has to be solved:

$$\dot{\epsilon}_{ij} = \sum_{s=1}^{12} \frac{1}{2} (p_{ij}^s + p_{ji}^s) \dot{\gamma}_s. \quad (5)$$

Here p_{ij}^s is the orientation factor of a slip system s , defined by $p_{ij}^s = b_i^s n_j^s$, where \mathbf{b} and \mathbf{n} are the slip direction and slip plane normal unit vectors. A unique solution of the equation system (5) can be obtained when the relation between the deviatoric stress \mathbf{S} and the resolved shear stress τ_s is considered:

$$\tau_s = S_{ij} p_{ij}^s. \quad (6)$$

Then, with the help of Eqs. (4)–(6), we obtain:

$$\dot{\epsilon}_{ij} = \sum_{s=1}^{12} \frac{1}{2} (p_{ij}^s + p_{ji}^s) \tau_s^{0 \frac{1-m}{1-m}} S_{kl} p_{kl}^s |S_{nq} p_{nq}^s|^{\frac{1-m}{m}}. \quad (7)$$

As elasticity is neglected, there are five independent equations in (7), because of plastic incompressibility. The unknowns are the 5 independent components of the deviatoric stress tensor, which can be obtained from Eqs. (7) via a numerical solution (for this purpose, the Newton–Raphson technique was employed). Once \mathbf{S} is known, the slip distribution can be calculated by using Eqs. (6) and (4). The slip distribution determines the orientation changes of the crystal (see, for example, Tóth *et al.*, 1988; 1990) through the relation

$$\dot{\mathbf{T}} = \dot{\mathbf{\Omega}} \mathbf{T}, \quad (8)$$

where $\dot{\mathbf{\Omega}}$ is the rate of lattice rotation defined by

$$\dot{\Omega}_{ij} = \dot{d}_{ij} - \sum_{s=1}^{12} p_{ij}^s \dot{\gamma}_s, \quad (9)$$

and \mathbf{T} is the transformation matrix going from the sample to the crystal reference system.

Hardening was also accounted for in the simulations. It was done in the same way as in the work of Bronkhorst *et al.* (1992). It was simulated by varying the reference stresses τ_s^0 in the constitutive law Eq. (4):

$$\dot{\tau}_s^0 = \sum_p H_{sp} |\dot{\gamma}_p| \quad \text{with } s, p = 1, \dots, 12, \quad (10)$$

where the hardening matrix H_{sp} is defined by

$$H_{sp} = q_{sp} h_0 \left\{ 1 - \frac{\tau_p^0}{\tau_{\text{sat}}} \right\}^a. \quad (11)$$

The 12×12 q_{sp} matrix governs self as well as latent hardening. It is defined so that $q_{sp} = 1$ for coplanar systems, and for all other elements $q_{sp} = 1.4$. The hardening parameters in Eq. (11), i.e. h_0 , τ_{sat} (saturation stress in the slip systems) and the exponent a , can be obtained from several large strain simulations by reproducing the experimental stress strain curves. Bronkhorst *et al.* (1992) deduced the following parameters for compression of an OFHC copper: $h_0 = 180$ MPa, $\tau_{\text{sat}} = 148$ MPa and $a = 2.25$. The same parameters were employed also in the present work, except for one of them: as the present material is not an OFHC copper but a 5N one, the saturation stress τ_{sat} was lowered to account for the higher purity; $\tau_{\text{sat}} = 111$ MPa was used in the present simulations. This value of τ_{sat} was obtained by reproducing the experimental flow stress value only in one point of one of the curves presented in Fig. 3. For the initialization of the reference resolved shear stresses in Eq. (10), the value of $\tau_s^0 = 16$ MPa was prescribed to each slip system before deformation started.

Simulation Results

The velocity gradient for 100 increments was calculated and implemented into the crystal plasticity code to obtain the orientation changes as well as the stress states as the crystal passes each die subsequently. In order to compare the predicted hardening state with the measured one, an equivalent stress quantity σ_{eq} was defined with the help of the

von Mises equivalent strain rate $\dot{\epsilon}_{\text{eq}} = \left(\frac{2}{3} \dot{\epsilon}_{ij} \dot{\epsilon}_{ij}\right)^{1/2}$ and the rate of plastic work $\dot{W} = S_{ij} \dot{\epsilon}_{ij}$, so that σ_{eq} be work-conjugate to $\dot{\epsilon}_{\text{eq}}$:

$$\sigma_{\text{eq}} = \frac{\dot{W}}{\dot{\epsilon}_{\text{eq}}}. \quad (12)$$

The calculated equivalent stresses are presented in Fig. 3, as a function of the radius in the $[100]$ and $[010]$ directions, after the crystal passed 6 dies.

Because of plastic deformation the orientation of the crystal changes. As the velocity gradient depends on r , the variations in the crystal lattice orientations are also dependent on the radius. There is an angular dependence, too, however, because the orientation of the initial crystal with respect to the local flow line depends on the exact location of the flow line within the cross section. During the pole figure measurements, as the whole cross section is illuminated by X-rays, the measured pole figure has to be seen as an average one. It is possible however, to simulate this 'average' pole figure, with the help of the present crystal plasticity simulations. For this purpose, the final orientations after 8 passes were calculated along 19 radial directions, in radius increments of 0.05, these directions being separated by a distance of 5° . Then, taking into account the symmetry of the test, the pole figure construction was made on the projection plane having its normal parallel to the z axis. Evidently, the volume fraction of the

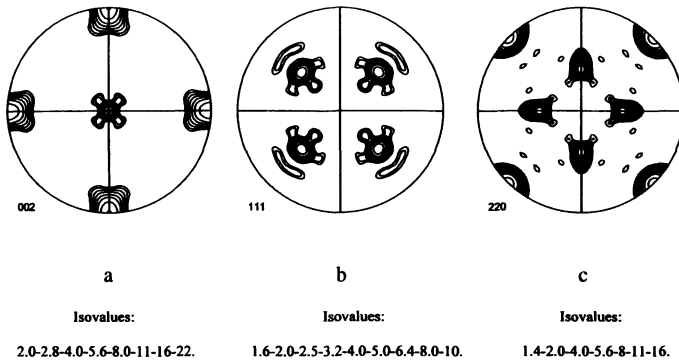


FIGURE 7 Simulated pole figures obtained from the crystal plasticity code after 8 passes (strain: $e = 1.41$): (a) $\{002\}$, (b) $\{111\}$ and (c) $\{220\}$.

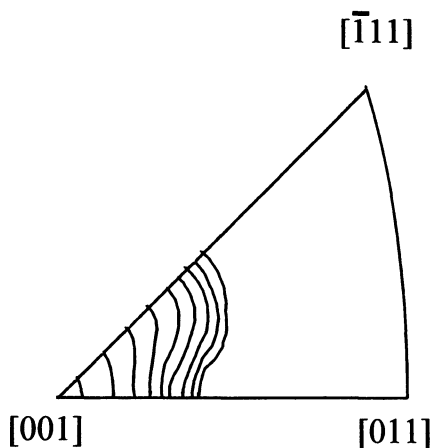


FIGURE 8 Simulated inverse pole figure for the sample deformed by 8 passes (strain: $e = 1.41$).

grains at different radial distances is not the same. It varies with r^2 , which was correctly taken into account in the construction of the simulated pole figures. The pole figures obtained in this way are displayed in Fig. 7. In order to analyze the orientation changes, an inverse pole figure has also been constructed, the one displaying the distribution of the longitudinal axis in the crystal reference system (Fig. 8).

DISCUSSION

As can be seen from a comparison of the measured and simulated hardening curves (see Fig. 3), the simulation reproduces well the experimental observations. The increase of the flow stress with the radius is correctly reproduced. The same is valid for the angular dependence. The variation of the flow stress is not too big along the radius, but it is definitely increasing. In order to clarify the origin of this variation, the strain distribution has been calculated along the $[100]$ and $[110]$ directions as a function of the radius. More precisely, the macroscopic and microscopic strains were calculated separately. The macroscopic one can be readily obtained from the imposed velocity gradient and it is represented by the von Mises accumulated strain after 6 passes in Fig. 9. Evidently, it does not have an angular dependence,

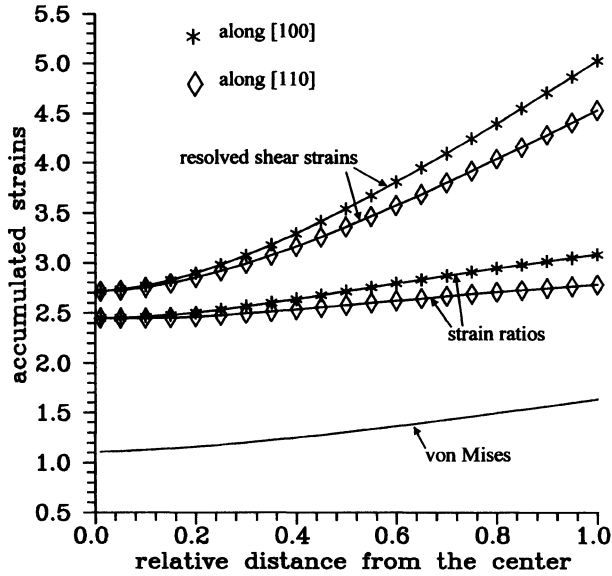


FIGURE 9 Accumulated microscopic slip (resolved shear strain) and macroscopic strains (von Mises), as well as their ratio, as a function of the radius after 6 passes along the [100] and [110] directions, as predicted from crystal plasticity (strain: $e = 1.41$).

because of symmetry. It shows a continuous increase as a function of the radius. The origin of this dependence is that the shear component of the prescribed strain increases with the radius. In fact, as it is clear from Eq. (2), the progression of the material along different flow lines is the same (as v_z is independent of r), that is, a plane perpendicular to the z axis remains a plane during deformation. Therefore, along all flow lines, the normal components of the imposed strain are the same. There is difference only in the shear component, which explains the increase in the accumulated von Mises strain as a function of the radius.

The origin of hardening, however, is crystallographic slip in the present modeling, as described earlier. For this reason, the accumulated resolved shear strain – which is defined as the sum of all crystallographic slips – has also been calculated and displayed in Fig. 9. As can be seen from this figure, the accumulated resolved shear strain increases considerably as a function of the radius in both the [100] and [110] directions. As it is expected, there is more increase in the [100] direction than in the [110]. The ratio of the two kinds of accumulated

strains (which could be called a kind of Taylor factor) also increases with r (see Fig. 9). Near $r = 0$, however, the total slip is the same in both directions, which apparently seems to be in contradiction with the differences predicted between the flow stresses (see Fig. 3). The reason for this resides in the differences in the stress states. More precisely, there is a significant difference in the shear stresses which are associated with the imposed shear component, $\dot{\epsilon}_{rz}$. Although this strain rate component is the same for both cases, as the orientations are not the same, there is a difference in the stress state, thus in the equivalent stresses.

The predicted pole figures (Fig. 7) show also a good agreement with the measured ones (Fig. 5). The cross-shaped maxima are well reproduced in the simulations. Close inspection of the obtained lattice rotations reveals that the crystal rotates more at larger radial positions, and the rotation depends also on the angular position. In all cases, however, the rotation takes place around the local tangential axis. It can be readily verified that the crystal would not rotate in the absence of the velocity gradient component \dot{d}_{rz} , that is, without the presence of the shear component. This component produces rotations in the sense of the shear, which is negative at the entrance of the die and becomes positive after the material passed the middle point and approaches the exit. The net rotation is not null and accumulates progressively. In fact, the net lattice rotation is maximum along the radius parallel to $[1\ 1\ 0]$, and zero along the radius $[1\ 0\ 0]$. As the rotation takes place around a local tangential axis, this leads to a shift of the reflection peaks and produces cross-shaped reflections in the pole figures as it can be seen in Figs. 5 and 7. In the inverse pole figure of the longitudinal axis, the above rotations promote mostly an elongation of the intensity distribution along the $[00\ 1] - [\bar{1}\ 1\ 1]$ line of the unit triangle (see Fig. 8).

Ahlborn (1966) found that in copper at very large area reductions, the two ideal positions are the $[00\ 1]$ and $[\bar{1}\ 1\ 1]$. When the initial orientation is a single crystal, however, only one of them can appear, depending on the initial orientation. In our experiments, the pole figures show the maximum intensity in the $[00\ 1]$ position, suggesting in this way that this is a stable orientation. Nevertheless, its intensity decreases as a function of strain. The simulations reveal some tendency of rotation of the drawing axis in the direction of $[\bar{1}\ 1\ 1]$ (see Fig. 8).

It does not mean, however, that the $[\bar{1} 1 1]$ orientation can develop from the initial $[0 0 1]$ at larger strains. We have carried out further simulations, up to an area reduction of 99%. The results obtained show that the stable orientation is still the $[0 0 1]$, the patterns of the predicted pole figures stay essentially the same, there is only a slight increase in the peak intensities.

Concerning the deformation bands which were seen experimentally and presented in Fig. 1, the following comments can be made. The origin of the deformation bands may be related to the differences between the boundary conditions imposed by the die and the symmetry elements of the crystal. The macroscopic deformation has cylindrical symmetry, while the crystal displays a four-fold symmetry around the axis of drawing, which is well reflected by the position of the deformation bands which are oriented perpendicularly to the $[0 0 1]/[0 1 0]$ directions. Ahlborn (1965a,b; 1966) has also shown in several examples that the deformation band pattern depends on the initial orientation of the crystal and presents the same symmetry elements. According to the present authors, the appearance of the deformation bands may be related to the changes in the slip system activity. Due to the crystal structure, the operating slip systems have to change as a function of the angular position. According to the present crystal plasticity simulations, there is only a certain angular interval around the $[1 0 0]$ and $[0 1 0]$ directions, where the same slip systems operate, only their relative activity varies to accommodate the prescribed deformation. However, as the angular position approaches 45° or 135° , there is a change in the slip systems. This is because another combination of slips is necessary to accommodate the prescribed deformation. This changeover in slip system activity facilitates the instabilities which may develop at the interface between these regions and may lead to the initiation of the observed deformation bands.

CONCLUSIONS

$[0 0 1]$ oriented copper single crystals were cold drawn up to true strains of about 1.41. The deformed structure was characterized by metallographic investigations, microhardness and texture measurements. To understand more the wire drawing process, crystal plasticity

simulations have also been carried out to follow the hardening variations as well as the orientation changes. From the obtained experimental as well as simulation results, the following main conclusions can be drawn:

1. During wire drawing of [00 1] oriented copper single crystals, the local orientation of the crystal varies due to a shear component. The measured (1 0 0) and (1 1 1) *average* pole figures in the cross section projection plane show cross-shaped maxima at a strain of $e = 1.41$.
2. The measured microhardness increases in the cross section as a function of the radius. The flow stress are significantly higher in the $\langle 100 \rangle$ directions compared to those measured along the $\langle 110 \rangle$ directions. Several deformation bands also develop, which are oriented perpendicular to the $\langle 100 \rangle$ directions.
3. The flow line model of Altan *et al.* (1992) describes well the deformation of the material through the die as it leads to good agreements with the measured results when it is used in conjunction with crystal plasticity calculations.
4. The viscoplastic crystal plasticity model including microscopic hardening can be used efficiently to model the microstructural changes (hardness and texture at the same time) in wire drawing of [00 1] oriented copper single crystals.

Acknowledgements

A. Borbély acknowledges with gratitude the fellowship granted by the Soros Foundation, Budapest, which made it possible to carry out the experiences at the University of Metz. The authors are grateful to Mrs. J. Pokorny and Dr. A. Pokorny (University of Metz) for their valuable help in the metallographic investigations and also to Prof. Heizmann (University of Metz), for the useful discussions. The collaboration with SODETAL (France) is also appreciated.

References

- Ahlborn, H., *Z. Metallkde.* (1965a), **56**, 205–15.
Ahlborn, H., *Z. Metallkde.* (1965b), **56**, 411–20.
Ahlborn, H., *Z. Metallkde.* (1966), **57**, 877–84.
Ahlborn, H. and Sauer, D., *Z. Metallkde.* (1968), **59**, 658–63.
Altan, S.B., Antar, N. and Gultekin, E., *J. Mat. Proc. Techn.* (1992), **33**, 263–72.

- Bronkhorst, C.A., Kalidindi, S.R. and Anand, L., *Phil. Trans. Royal Soc. London* (1992), **A328**, 443–56.
- Heizmann, J.J., Tóth, L.S. and Abdellaoui, A., *Proc. ICOTOM 11*, Eds. Z. Liang, L. Zuo and Y. Chu, Xi'an, China, 16–20 Sept. (1996), pp. 274–279.
- Van Houtte, P., Watté, P., Aernoudt, E., Gil Sevillano, J., Lefever, I. and Van Raemdonck, W., *Materials Science Forum* (1994), **157–162**, 1881–86.
- Hutchinson, J.W., *Proc. Roy. Soc. Lond. A* (1976), **348**, 101–27.
- Mathur, K.K. and Dawson, P.R., *Transactions of the ASME* (1990), **112**, 292.
- Molinari, A., Canova, G.R. and Ahzi, S., *Acta metall.* (1987), **35**, 2983–94.
- Montesin, T., Heizmann, J.J. and Pelletier, J.B., *Wire J. Int.* (1991), **24**, 56–64.
- Pokorny, A. and Pokorny, J., *De Ferri Metallographia*, Berger-Levrault, Paris, Nancy (1967).
- Gil Sevillano, J., Van Houtte, P. and Aernoudt, E., *Progr. Mater. Sci.* (1980), **25**, 69–412.
- Sugondo, Szpunar, J.A. and Gangli, P., *J. Mat. Sci. Proc. Techn.* (1991), **16**, 305–14.
- Tabor, D., *J. Inst. Metals* (1951), **79**, 1–18.
- Taylor, G.I., *J. Inst. Metals* (1938), **62**, 307–24.
- Tóth, L.S., Gilormini, P. and Jonas, J.J., *Acta metall.* (1988), **36**, 3077–91.
- Tóth, L.S., Jonas, J.J., Gilormini, P. and Bacroix, B., *Int. J. Plasticity* (1990), **6**, 83–95.

APPENDIX

The 4 non-null components of the velocity gradient can be obtained by derivation of the velocities (Eq. (2)) in cylindrical coordinates. They are:

$$\begin{aligned}\dot{d}_{rr} &= -v_f E^2 \frac{6z(A-z)}{F^3}, \\ \dot{d}_{rz} &= -\frac{6v_f r E^2 [18z^2(A-z)^2 - (A-2z)F]}{F^4}, \\ \dot{d}_{\theta\theta} &= \dot{d}_{rr}, \quad \dot{d}_{zz} = -2\dot{d}_{rr},\end{aligned}$$

where

$$E = \frac{R_2 A^3}{R_1 - R_2}, \quad F = z^2(3A - 2z) + E.$$

The time necessary to pass through the die is obtained by an integral of the velocity component v_z :

$$t = \frac{A}{v_f} \left[\frac{13}{35} \left(\frac{R_1}{R_2} - 1 \right)^2 + \frac{R_1}{R_2} \right].$$